Applied Catalysis B: Environmental 256 (2019) 117845

Contents lists available at ScienceDirect

Applied Catalysis B: Environmental

journal homepage: www.elsevier.com/locate/apcatb

Mechanism of the CO_2 storage and in situ hydrogenation to CH_4. Temperature and adsorbent loading effects over Ru-CaO/Al_2O_3 and Ru-Na_2CO_3/Al_2O_3 catalysts

A. Bermejo-López, B. Pereda-Ayo, J.A. González-Marcos, J.R. González-Velasco*

Department of Chemical Engineering, Faculty of Science and Technology, Universidad del País Vasco UPV/EHU, Barrio Sarriena, s/n, 48940 Leioa, Bizkaia, Spain

ARTICLE INFO

Keywords:
CO_2 hydrogenation
CO_2 storage
Methanation
Dual function material
Ruthenium

ABSTRACT

The use of fossil fuels to satisfy the growing energy demand results in the emission of a huge amount of CO_2 to the atmosphere. One alternative to overcome this environmental issue is the CO_2 valorization through the storage and in situ hydrogenation to CH_4. In this work, Ru-CaO/Al_2O_3 and Ru-Na_2CO_3/Al_2O_3 dual function materials are synthesized with different adsorbent loadings, namely 5, 10 and 15 wt.%. The prepared catalysts are characterized in terms of surface area by N_2 adsorption and desorption, crystallinity by XRD, Ru dispersion by H_2-chemisorption and TEM, basicity by CO_2-TPD and reducibility and oxidation state of the noble metal by H_2-TPR and XPS. Temperature programmed surface reaction experiments with H_2 on samples with pre-adsorbed CO_2 reveal that the decomposition of surface carbonates and the subsequent hydrogenation occurs at lower temperatures for catalysts containing Na_2CO_3 than CaO. A complete reaction scheme describing the CO_2 adsorption and hydrogenation process has been proposed based on the temporal evolution of reactants and products. Oxides (CaO or Na_2O) and hydrated oxides ($Ca(OH)_2$ or NaOH) have been identified as CO_2 storage sites, the former oxides being more reactive towards the CO_2 adsorption. CH_4, H_2O and minor amounts of CO are detected during the hydrogenation step. The CO_2 storage and hydrogenation to CH_4 is promoted with increasing the adsorbent loading. Maximum CH_4 production of 414 μmol g^{-1} is observed for Ru15%CaO/Al_2O_3 at 400 °C. High temperature is needed to efficiently decompose the highly stable carbonates formed onto CaO. On the other hand, the higher Ru dispersion along with a lower stability of carbonates in Ru10%Na_2CO_3/Al_2O_3 promotes CH_4 formation (383 μmol g^{-1}) at notably lower temperature, i.e. 310 °C. Thus, Ru10%Na_2CO_3/Al_2O_3 is regarded as a suitable catalyst for the CO_2 storage and in situ hydrogenation to CH_4.

1. Introduction

The growing increase in energy demand is causing the increase of emissions of gaseous pollutants into the atmosphere, such as greenhouse gases, mainly CO_2 [1]. This fact, together with a greater social awareness, is leading to the need of developing processes and materials to reduce these emissions [2–5].

Natural gas or coal-fired power plants emit significant amounts of CO_2 into the atmosphere and carbon emission taxes are starting to be implemented in industrially developed countries. In order to reduce environmental pollution and avoid emission taxes, there are basically two strategies: i) capturing and storing the CO_2 and ii) recycling and recovering the CO_2 [6,7]. Technologies for the sequestration and geological storage of CO_2 are expensive and energetically unsustainable [8], so that using CO_2 as a carbon source, instead of emitting it as a waste, is a promising and attractive alternative. In this approach, a worthless compound as CO_2, can be converted into commercial chemicals or combustibles [9].

The valorization of CO_2 is challenging, since the transformation of carbon dioxide into chemical products makes sense only if using renewable energies and renewable raw materials. The hydrogenation of CO_2 leads to a large variety of products such as methane [10], methanol [11], carbon monoxide [10] and formic acid [12]. Dry reforming of methane (DRM) is also considered one of the most-important pathways for the production of methanol and a variety of other liquid fuels by the Fischer-Tropsch process [13–15]. Among the different conversion alternatives, the methanation of CO_2 is the most favored reaction by the thermodynamics. Carbon dioxide, captured from the gas effluent of a combustion processes, can react catalytically with renewable H_2 to produce synthetic natural gas (SNG), by the reaction of Sabatier [16]:

* Corresponding author.
E-mail address: juanra.gonzalezvelasco@ehu.eus (J.R. González-Velasco).

https://doi.org/10.1016/j.apcatb.2019.117845
Received 10 April 2019; Received in revised form 5 June 2019; Accepted 7 June 2019
0926-3373/ © 2019 Elsevier B.V. All rights reserved.

$$CO_2 + 4H_2 \leftrightarrows CH_4 + H_2O \quad \Delta H = -164\ kJ/mol \qquad (1)$$

This alternative is a promising option already demonstrated at industrial scale in an "e-gas" plant of the Audi Motor company in Werlte (Germany), which produces 1000 tm of SNG per year from a concentrated CO_2 feed stream obtained in a nearby biogas plant [17].

Studies have been conducted on different catalyst formulations for CO_2 methanation, including group VIIIB metals (Fe, Ru, Co, Rh, Ir, Ni, Pd, Pt) supported on several oxides (SiO_2, TiO_2, Al_2O_3, ZrO_2, CeO_2, and mixed oxides Ce-Zr) [18–23]. Ru and Rh have been reported as the most active metals for the selective hydrogenation of CO_2 to CH_4 [24].

The concept of producing chemicals and fuels directly from industrial flue gases over a dual function material (DFM) has been previously applied to the production of syngas (CO and H_2), a useful reactant for methanol synthesis [15,25,26]. In this process (tri-reforming of methane), a synergetic combination of CO_2 reforming, steam reforming, and partial oxidation of methane occurs in a single reactor at 850 °C with supported nickel catalysts.

Recently, the use of DFMs to achieve CO_2 methanation from diluted streams without needing a previous stage of sequestration and concentration has been published for the first time in the scientific literature [27]. The DFMs contain an alkaline or alkaline earth metal that adsorb CO_2 and a noble metal to promote the methanation reaction. These materials allow CO_2 storage and direct conversion to methane without the need for energy intensive thermal CO_2 purification processes. In this aproach, when the catalyst is saturated with CO_2 and H_2 is injected, a spillover phenomenon occurs that leads the chemisorbed CO_2 to the catalytic centers of the noble metal where the methanation occurs. This fact means that the energy requirement of the process is limited to obtaining H_2, and therefore, the CO_2 capture process, conversion to CH_4 and subsequent use of the fuel approximates a CO_2 neutral cycle, with no net emissions from this gas to the atmosphere. This requires obtaining hydrogen from a renewable energy source.

Other configurations have been studied later on for the combined CO_2 capture and catalytic conversion to methane. Veselovskaya et al. studied the possibility of performing the capture and methanation in physically separated stages [28,29]. The advantage of this configuration is the possibility to optimize the two processes of capture and methanation, for example in terms of temperature and pressure [30]. Later studies evaluated the feasibility of performing the capture and methanation process in the same physical unit using two different solids [31,32]. The advantage of this configuration is the lower investment cost (only one reactor for both processes). Also, the preparation of both types of solids can be optimized separately, in a search for high adsorption or methanation performance [30]. Even so, a unique reactor configuration using DFMs obtains better results due to the close proximity between the basic storage sites for CO_2 adsorption and metallic sites for hydrogenation, both impregnated onto the same support.

Both the CO_2 capture process and the CH_4 conversion process can operate at 300–400 °C, a temperature that can be supplied by heat recovered from the emission stream, without the need of external heat input. The DFM is placed in two parallel reactors which operate alternating CO_2 storage and hydrogenation cycles.

Farrauto's group has been pioneer in the development of DFMs for the CO_2 storage and hydrogenation to CH_4 [27,33,34]. Ru-CaO/Al_2O_3 was first proposed as an efficient catalyst to assist the reaction and the influence of the preparation method and reaction conditions were analyzed. Thereafter, K_2CO_3 and Na_2CO_3 were proposed as alternative sorbent materials, which ultimately increased the methanation capacity with respect to the conventional CaO. Alternative catalysts to those based on noble metals have also been proposed, e.g. in FeCrCu-K-MgO/Al_2O_3 catalyst [35]. More recently, parametric and cycling aging studies using Na_2CO_3 as adsorbent have been reported [36].

In the current paper, we are presenting an extensive study on the evolution of physico-chemical properties of Ru-CaO/Al_2O_3 and Ru-Na_2CO_3/Al_2O_3 catalysts with increasing adsorbent loadings, which to our knowledge has not been reported yet in the literature. We also analyze the temporal evolution of reactants and products, i.e. CO_2, CO, H_2O and CH_4 during the CO_2 storage and hydrogenation cycles. Based on these results, we propose a complete reaction mechanism validated on experimental evidences. Differences in the catalytic performance towards the CO_2 adsorption and hydrogenation at different temperatures (280–400 °C) are correlated with the physico-chemical properties of the prepared catalysts.

2. Experimental

2.1. Catalyst preparation

All samples were prepared by wetness impregnation. First, appropriated amount of $Ca(NO_3)_2{\cdot}H_2O$ (Sigma Aldrich, purity 99.99%) or Na_2CO_3 (Riedel de-Haën, purity 99.9%) was impregnated over γ-Al_2O_3 (Saint Gobain). The impregnated powder was dried at 120 °C overnight and then calcined in air at 400 °C to decompose the precursor salt. Afterwards, $Ru(NO)(NO_3)_2$ (Sigma Aldrich) was impregnated over xCaO/Al_2O_3 or xNa_2CO_3/Al_2O_3 (x = 5, 10 and 15%). This impregnation sequence, i.e. the adsorbent and then the noble metal, has been reported to achieve better catalytic performance [27] and was also verified in this work, as reported in the supplementary material (Figure S1). After drying at 120 °C, the samples were stabilized by calcining again at 400 °C in air for 4 h. The supplementary material also collects preliminary results about the utilization of sodium nitrate instead of carbonate as precursor.

2.2. X Ray Diffraction (XRD)

X-ray diffraction patterns were obtained in a *Philips PW1710* diffractometer. The samples were finely ground and were subjected to Cu Kα radiation in a continuous scan mode from 5° to 70° 2θ with 0.02 per second sampling interval. *PANalytical X'pert HighScore* and *Winplotr* profile fitting software were used for data treatment.

2.3. N_2 adsorption-desorption

The N_2 adsorption-desorption analysis were carried out at the nitrogen boiling temperature (−196 °C) using an automated gas adsorption analyser (*TriStar II, Micromeritics*). The samples were purged with nitrogen for 10 h at 300 °C using *SmartPrep degas system* (*Micromeritics*).

2.4. H_2 chemisorption

Ruthenium dispersion was determined using the H_2 chemisorption method in a *Micromeritics ASAP 2020* equipment. The catalyst (0.35 g) was first outgassed at 300 °C for 60 min and reduced in 50 ml min^{-1} of 5% H_2/Ar at 350 °C during 2 h. Then, the sample was furher outgassed at 360 °C for 90 min. Finally, H_2 was dossed for obtaining the adsorption isotherm at 35 °C. Before repeating the adsorption isotherm, the sample was again outgassed for 60 min, and the difference between first and second isotherms was related with the amount of H_2 chemisorbed on the catalyst surface.

2.5. Transmission electron microscopy (TEM)

The morphology of the samples was analysed by transmission electron microscopy (TEM) in a *Philips CM200* transmission electron microscope with a LaB6 filament as the source of electrons operated at 200 kV. The samples were dispersed in absolute ethanol ultrasonically, and the solutions were then dropped on copper grids coated with lacey carbon film.

Table 1
Nomenclature, adsorbent loading and textural properties of the prepared catalysts and the reference materials.

Sample	Nomenclature	Adsorbent wt.%	S_{BET}, m^2/g	d_p, Å	V_p, cm^3/g
γ-Al_2O_3	Al_2O_3	–	217.3	107.5	0.60
4% Ru/Al_2O_3	Ru/Al_2O_3	–	198.6	103.3	0.53
10% CaO/Al_2O_3	$10CaO/Al_2O_3$	10% CaO / 17.9% $CaCO_3$	181.3	99.4	0.47
10% Na_2CO_3/Al_2O_3	$10Na_2CO_3/Al_2O_3$	5.8% Na_2O / 10% Na_2CO_3 / 15.8% $NaHCO_3$	184.5	109.0	0.52
4% Ru 5% CaO/Al_2O_3	Ru5CaO	5% CaO / 8.9% $CaCO_3$	193.2	100.6	0.50
4% Ru 10% CaO/Al_2O_3	Ru10CaO	10% CaO / 17.9% $CaCO_3$	170.9	99.8	0.45
4% Ru 15% CaO/Al_2O_3	Ru15CaO	15% CaO / 26.8% $CaCO_3$	148.4	99.1	0.39
4% Ru 5% Na_2CO_3/Al_2O_3	$Ru5Na_2CO_3$	2.9% Na_2O / 5% Na_2CO_3 / 7.9% $NaHCO_3$	194.2	101.1	0.52
4% Ru 10% Na_2CO_3/Al_2O_3	$Ru10Na_2CO_3$	5.8% Na_2O / 10% Na_2CO_3 / 15.8% $NaHCO_3$	164.7	103.5	0.45
4% Ru 15% Na_2CO_3/Al_2O_3	$Ru15Na_2CO_3$	8.8% Na_2O / 15% Na_2CO_3 / 23.8% $NaHCO_3$	119.6	116.6	0.36

2.6. Temperature-programmed reduction (H_2-TPR)

The reducibility of the samples was investigated by temperature programmed reduction (H_2-TPR) in a Micromeritics AutoChem II equipment. The quartz tube reactor was loaded with 0.1 g of sample, which was pretreated with 5% O_2/He at 350 °C and then cooled down to 35 °C. Afterwards, samples were heated from RT to 950 °C at of 10 °C min^{-1} in 5% H_2/Ar stream with a flowrate of 30 ml min^{-1}. Water generated during samples reduction was removed using a cold trap before the gas was analyzed which a TCD detector. For some experiments, the effluent gas was also analyzed in a MultiGas 2030 FT-IR analyzer to quantify the formation of products during the reduction.

2.7. Temperature-programmed desorption (CO_2-TPD)

The CO_2-TPD experiments were carried out in a *Micromeritics AutoChem II* equipment. The samples (0.1 g) were pretreated at 400 °C under He and then cooled down to 35 °C. Thereafter, samples were heated from RT to 350 °C at 10 °C min^{-1} in a 5% H_2/Ar stream with a total flowrate of 50 ml min^{-1} until a complete reduction of the samples before the experiment. Subsequently, the samples were exposed to a gas stream composed of 5% CO_2/He at 30 ml min^{-1} for 1 h at RT to saturate the catalyst with CO_2. Then, the samples were exposed to He for 90 min to remove the physically adsorbed CO_2. Finally, the samples were heated from RT to 900 °C at 10 °C min^{-1} and the CO_2 released was measured by mass spectrometry (*OMNI StarTM*).

2.8. Temperature programmed surface reaction (TPSR)

The TPSR experiments were carried out in a quartz tube reactor placed in a horizontal furnace. The sample (0.3 g) was pretreated under 5% H_2/Ar at 400 °C until the complete reduction of ruthenium, and then, the sample was cooled down to 50 °C. Subsequently, the samples were exposed to a gas stream composed of 28% CO_2/Ar with a flowrate of 700 ml min^{-1} for 20 min at 50 °C to saturate the catalyst with CO_2. Afterwards, the samples were heated from 50 to 600 °C at 10 °C min^{-1} in a 5% H_2/Ar mixture with a flowrate of 700 ml min^{-1}. The MultiGas 2030 FT-IR analyzer was used to quantify the formation of products during the reduction in the reactor effluent gas.

2.9. Reactor testing

The catalytic activity of the samples was evaluated in a vertical stainless steel tubular reactor loaded with 1 g of pelletized (0.3-0.5 mm) catalyst. Prior to the analysis, the sample was reduced under 10% H_2/Ar at 350 °C for 45 min. During the storage step, 1.4% CO_2/Ar or 11% CO_2/Ar was fed for 1 min, followed by a purge with Ar for 2 min to remove the weakly adsorbed CO_2. Then, during the hydrogenation step, 10% H_2/Ar was fed for 2 min, followed by a purge with Ar for 1 min before starting again the storage step. Throughout the experiment, the total flow rate was 1200 ml min^{-1}, which corresponds to a GHSV of 45.000 h^{-1}. The experiments were carried out in the temperature range between 280 and 400 °C.

The composition of the exhaust gas was continuously analyzed using the MultiGas 2030 FT-IR analyzer for the quantitative analysis of CO_2, CH_4, CO and H_2O. The CO_2 adsorption capacity during the storage step was calculated with Eq. (2), whereas the amount of CH_4, CO and H_2O produced during the hydrogenation step was calculated with Eq. (3),(4) and (5), respectively. Definitive catalytic parameters were calculated as average values of three consecutive cycles.

$$\text{Stored } CO_2\,(\mu mol\,g^{-1}) = \int_0^{ts} [F_{CO2}^{in} - F_{CO2}^{out}(t)]dt \quad (2)$$

$$CH_4\,(\mu mol\,g^{-1}) = \int_0^{tH} F_{CH_4}^{out}(t)dt \quad (3)$$

$$CO\,(\mu mol\,g^{-1}) = \int_0^{tH} F_{CO}^{out}(t)dt \quad (4)$$

$$H_2O\,(\mu mol\,g^{-1}) = \int_0^{tH} F_{H_2O}^{out}(t)dt \quad (5)$$

3. Results and discussion

3.1. Structural properties of the prepared catalysts

The nomenclature and structural properties of the prepared catalysts, together with the corresponding reference materials, are summarized in Table 1. The adsorbent loading has been expressed as a function of the chemical nature, i.e. oxide (CaO or Na_2O), carbonate ($CaCO_3$ or Na_2CO_3) and bicarbonate in the case of sodium ($NaHCO_3$). The reference material for the adsorption of CO_2 has been considered CaO and Na_2CO_3. The specific surface area of the γ-Al_2O_3 was found to be 217 $m^2\,g^{-1}$. The incorporation of the adsorbent, i.e. 10%CaO/Al_2O_3 or 10%Na_2CO_3/Al_2O_3, decreased significantly the specific surface area to 181 and 184 $m^2\,g^{-1}$, respectively, attributed to the partial blocking of the pores of the support [37]. In the same line, the incorporation of ruthenium to the alumina, i.e. 4%Ru/Al_2O_3, also produced a decrease in the exposed surface area but in a minor extent (199 $m^2\,g^{-1}$). As expected, when the adsorbent and the noble metal are successively impregnated over the alumina support, the specific surface area is further penalized. For example, the incorporation of Ru over 10%CaO/Al_2O_3, i.e. 4%Ru10%CaO/Al_2O_3, decreased the specific surface area to 171 $m^2\,g^{-1}$. The adsorbent content has a notable impact in the specific surface area. The higher the adsorbent loading, the lower the surface area is. Specifically, sodium carbonate penalizes in a greater extent the exposed surface area with respect to calcium oxide, i.e. 120 $m^2\,g^{-1}$ vs. 148 $m^2\,g^{-1}$, respectively, for an adsorbent content of 15%. Similar conclusions can be extracted from the evolution of the total pore volume. No significant changes can be observed in the average pore diameter after the incorporation of the noble metal and the adsorbent.

Fig. 1 shows the most representative XRD profiles of the synthesized samples. All the samples presented some diffraction peaks attributed to one or more crystalline structures. Wide diffraction peaks with low

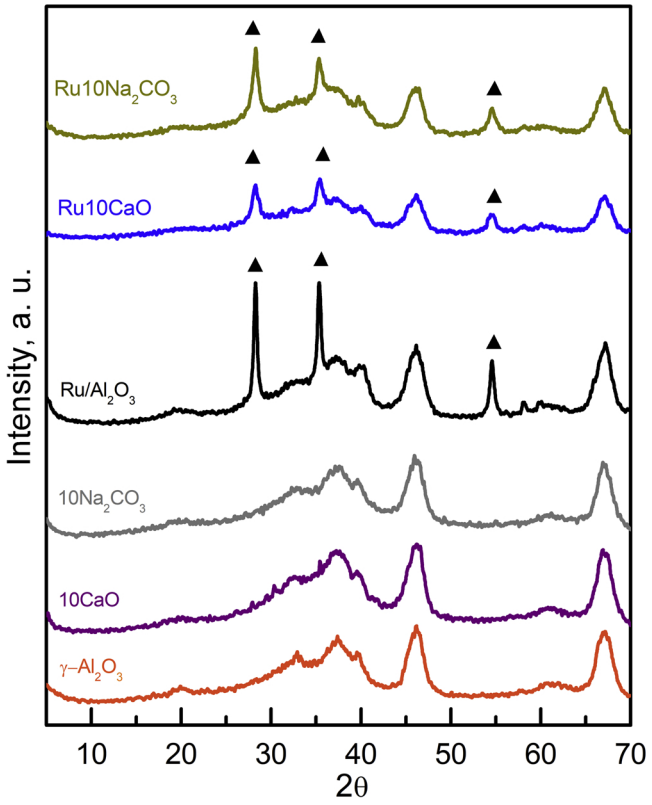

Fig. 1. XRD diffraction patterns for Ru10CaO and Ru10Na_2CO_3 together with reference samples. Diffraction peaks belonging to RuO_2 are identified with solid triangles (▲).

intensity, characteristic of γ-Al_2O_3, are observable in all samples. The XRD patterns of 10%CaO/Al_2O_3 and 10%Na_2CO_3/Al_2O_3 samples slight differ from that of bare alumina, which means that the adsorbents do not form a crystalline structure probably because they are well dispersed over the alumina support. Even for the samples containing the highest adsorbent loading (15%), diffraction peaks belonging to CaO or Na_2CO_3 are not detected (Figure S2). These results are in agreement with those obtained by Zhao et al. [38] who did not appreciate peaks of Na_2CO_3 up to a 25 wt.% and by Pasupulety et al. [39] who neither appreciate peaks for the sample 20% CaO/Al_2O_3. On the contrary, three intense peaks belonging to RuO_2 (▲) are distinguished for all the samples containing ruthenium as also reported by Tada el al. [40].

3.2. Ru dispersion

Ruthenium dispersion has been estimated by H_2-chemisorption considering a chemisorption stoichiometry of H/Ru = 1 [41,42] resulting in the values collected in Table 2. Modest ruthenium dispersion is obtained for all the prepared catalysts. For the catalysts containing CaO as adsorbent, a maximum Ru dispersion of 13% is obtained for 4% Ru5%CaO/Al_2O_3. Ru dispersion is progressively reduced while the adsorbent loading is increased, resulting in 11% and 9% for CaO loadings of 1 0 wt.% and 15 wt.%, respectively. This trend could be expected due to the progressive surface area reduction as increasing the adsorbent content (see Table 1). The dispersion of the noble metal is more challenging with a lower exposed surface area. On the contrary, for the catalysts containing Na_2CO_3 as adsorbent, a maximum Ru dispersion of 19% is obtained for the sample with the highest loading of adsorbent, i.e. 4%Ru15%Na_2CO_3/Al_2O_3. Ru dispersion is reduced to 18% and 12% for Na_2CO_3 loadings of 10 wt.% and 5 wt.%, respectively. Thus although increasing loadings of Na_2CO_3 penalized the exposed surface area, the dispersion of Ru was favored.

Table 2
Ru dispersion estimated by H_2 chemisorption, Ru particle size derived from the dispersion value and from TEM micrographs.

Sample	Ru disp, %	d_c (chem), nm	d_c (TEM), nm
Ru5CaO	13.1	10.1	9.2
Ru10CaO	11.5	11.5	9.6
Ru15CaO	9.5	13.9	10.8
Ru5Na_2CO_3	11.6	11.5	9.7
Ru10Na_2CO_3	18.7	7.1	8.2
Ru15Na_2CO_3	19.3	6.9	7.7

Transmission Electron Microscopy (TEM) was also employed to determine the size of Ru particles (Fig. 2). The darker spherical areas in the micrograph correspond to Ru [43,44], which was confirmed by EDX. The average particle size the Ru particles estimated by measuring the size of at least 100 particles and results are collected in Table 2. The particle sizes measured by TEM is follow same trend than particle sizes determined by H_2 chemisorption. The Ru particles tend to increase with the CaO content, increasing the heterogeneity and promoting the formation of larger aggregates. The opposite effect occurred for Na_2CO_3, the particle size was reduced with the adsorbent loading and Ru aggregates were not detected. Thus, TEM images confirmed that CaO loading penalizes Ru dispersion whereas Na_2CO_3 loading serves as a promoter.

3.3. Temperature-programmed experiments (CO_2-TPD and H_2-TPR)

The basicity of the prepared samples was determined by CO_2-TPD (Fig. 3). The samples with a low content of adsorbent (5 wt.%), either CaO or Na_2CO_3, illustrated a single CO_2 desorption peak at low temperature. On the contrary, the samples with a higher adsorbent loading (10 wt.% and 15 wt.%), either CaO or Na_2CO_3, presented two CO_2 desorption peaks at low and high temperature. The low temperature desorption peak is assigned to weakly or physically adsorbed CO_2 on the catalyst surface. The high temperature desorption peak is assigned to strongly adsorbed CO_2 forming stable carbonates (CO_3^{2-}) or bicarbonates (HCO_3-) [45].

As shown in Table 3, the weak basicity, comprising the amount of CO_2 desorbed below 400 °C, resulted in 287 μmol $CO_2\,g^{-1}$, whereas the strong basicity, comprising the amount of CO_2 desorbed above 400 °C, accounted for 110 μmol $CO_2\,g^{-1}$ for the sample containing 5 wt.% of CaO. Both the weak (477 μmol $CO_2\,g^{-1}$) and strong (472 μmol $CO_2\,g^{-1}$) basicity were enhanced when the adsorbent loading was increased to 10 wt.%, although the enhancement of the strong basicity was more pronounced. A further increase in the adsorbent loading up to 15 wt.% did not increase the weak basicity, in fact it was slightly reduced to (388 μmol $CO_2\,g^{-1}$). In contrast, the strong basicity was remarkably increased to (750 μmol $CO_2\,g^{-1}$). The low temperature desorption peak was centered at 120 °C irrespective of the adsorbent loading. However, the high temperature desorption peak was progressively moved to higher temperatures, i.e. 520, 630 and 680 °C, for increasing adsorbent loadings of 5, 10 and 15 wt.%, respectively. This fact indicates that the strength of the strong basicity progressively increases probably due to the formation of large CaO aggregates that adsorb CO_2 to form a stable $CaCO_3$ phase.

Similar conclusions can be extracted from Table 3 in the case of Na_2CO_3. The weak basicity is predominant in the case of low adsorbent loadings and strong basicity is promoted for higher loadings. However, some differences are also detected. First, the contribution of the weak basicity is notably higher for Na_2CO_3. Note that even for the highest adsorbent loading the weak basicity is predominant. Second, the strength of the strong basicity is lower for Na_2CO_3. The high temperature CO_2 desorption peak is centered at somewhat lower temperatures, i.e. 480, 560 and 640 °C, revealing that carbonates are not so stable than carbonates on CaO.

As metallic Ru and alumina are able to participate in the storage of

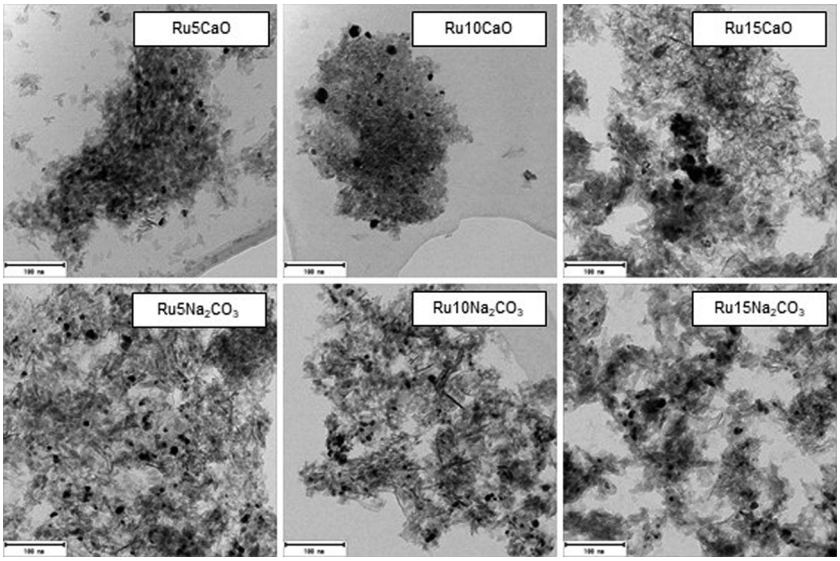

Fig. 2. TEM images for pre-reduced Ru-CaO/Al_2O_3 and Ru-Na_2CO_3/Al_2O_3 samples with different adsorbent contents, i.e. 5, 10 and 15 wt.%.

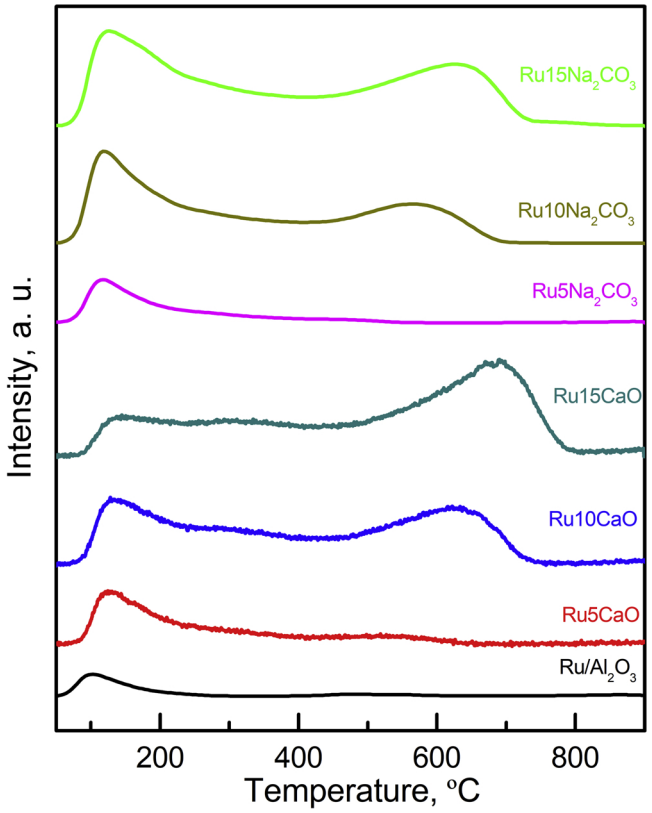

Fig. 3. CO_2-TPD patterns for pre-reduced Ru-CaO/Al_2O_3 and Ru-Na_2CO_3/Al_2O_3 samples with different adsorbent contents, i.e. 5, 10 and 15 wt.%. Ru/Al_2O_3 sample is also included as reference.

CO_2 [46] a specific experiment was carried out with the 4%Ru/Al_2O_3 sample. It was determined that this sample was able to store and then desorb 110 μmol CO_2 g^{-1}. Consequently, in order to calculate accurately the amount of CO_2 desorbed specifically from the adsorbent, the amount of CO_2 desorbed from the 4%Ru/Al_2O_3 sample was subtracted. Following this procedure, the ratio of desorbed moles of CO_2 per mol of adsorbent was calculated and is collected in Table 3.

Considering the decomposition reactions of calcium carbonate ($CaCO_3 \rightarrow CaO + CO_2$) and sodium carbonate ($Na_2CO_3 \rightarrow Na_2O + CO_2$)

Table 3
Weak, strong and total basicity of the prepared samples. The utilization of the adsorbent is also included in the last column.

Sample	Weak basicity, μmol CO_2 g^{-1}	Strong basicity, μmol CO_2 g^{-1}	Total basicity, μmol CO_2 g^{-1}	Adsorbent utilization
Ru5CaO	287	110	397	0.32
Ru10CaO	477	472	949	0.47
Ru15CaO	388	750	1138	0.38
Ru5Na_2CO_3	196	29	225	0.24
Ru10Na_2CO_3	503	299	802	0.73
Ru15Na_2CO_3	617	521	1138	0.72
Ru/Al_2O_3	86	24	110	–

*Weak basicity is determined as the moles of CO_2 desorbed below 400 °C.
* Strong basicity is determined as the moles of CO_2 desorbed above 400 °C.
* Adsorbent utilization is expressed as the moles of CO_2 desorbed per mol of adsorbent, CO_2/CaO or CO_2/Na_2CO_3.

one would expect 1 mol of CO_2 desorbed per mol of adsorbent, either CaO or Na_2CO_3, if the adsorbent was completely carbonated before the CO_2-TPD. As can be observed in Table 3, the ratio was situated below 1 for all the samples, indicating that the utilization of the adsorbent was not total. In the case of CaO, the (CO_2/CaO) ratio describes a maximum (0.47) for an adsorbent loading of 10 wt.%. The utilization of the adsorbent is lower, i.e. 0.32 and 0.38, for adsorbent loadings of 5 wt.% and 15 wt.%, respectively. In the case of Na_2CO_3, the utilization of the adsorbent is similar to $CaCO_3$ for an adsorbent loading of 5 wt.%, i.e. 0.24. However, the (CO_2/Na_2CO_3) ratio increases to 0.73 and 0.72 for Na_2CO_3 loadings of 10 and 15 wt.%, respectively, much higher than that observed for CaO. This higher utilization of the adsorbent could be due to a better dispersion of Na_2CO_3 or to the ability of sodium carbonate to form sodium bicarbonate. Indeed, the decomposition of sodium bicarbonate to sodium carbonate ($2NaHCO_3 \rightarrow Na_2CO_3 + H_2O + CO_2$) and the subsequent decomposition of sodium carbonate to sodium oxide ($Na_2CO_3 \rightarrow Na_2O + CO_2$) should led to the release of two molecules of CO_2. If the formation of sodium bicarbonate is considered, the utilization of the adsorbent results in values closer to CaO, i.e. 0.12, 0.37 and 0.36 for 5 wt.%, 10 wt.% and 15 wt.%, respectively.

Fig. 4 shows the H_2-TPR experiments for the prepared samples. A single reduction peak was observed for the reference 4%Ru/Al_2O_3 sample at 200 °C, assigned to the reduction of Ru_xO_y species to Ru^0. The samples containing CaO as adsorbent presented also a single reduction peak but progressively shifted to higher temperatures with increasing

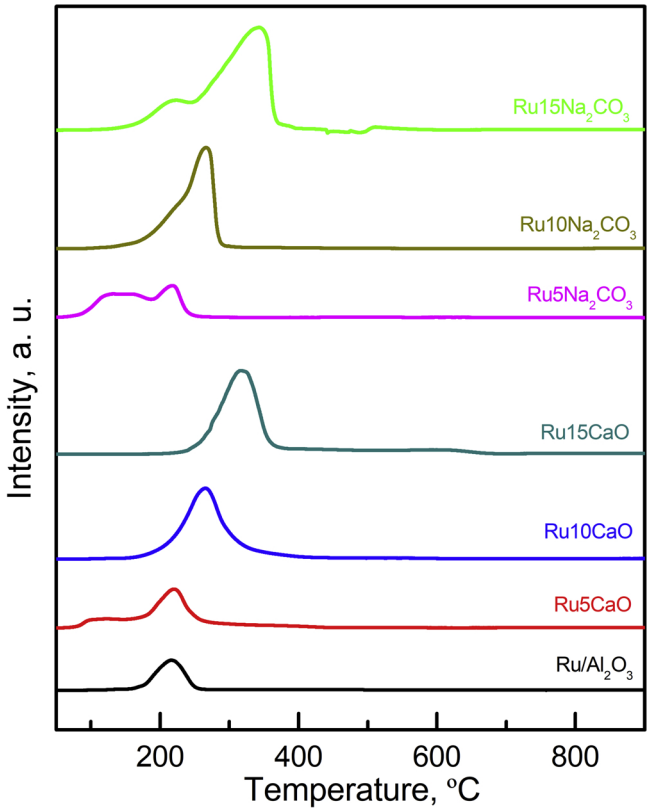

Fig. 4. H_2-TPR patterns for Ru-CaO/Al_2O_3 and Ru-Na_2CO_3/Al_2O_3 samples with different adsorbent contents, i.e. 5, 10 and 15 wt.%. Ru/Al_2O_3 sample is also included as reference.

the adsorbent loading. A progressive increase in the area under the peak was also observed. Considering that the unique reducible species in the catalyst is Ru and that the noble metal content is the same for all prepared samples, there should be an additional effect to explain the increase of the hydrogen consumption as the adsorbent loading increases.

In order to gain insight into the reduction process, the effluent gas of the H_2-TPR experiment was analyzed by FTIR to quantitatively determine the products of the reduction process. As can be observed in Figure S3, nitrogen and carbon containing products were detected during the H_2-TPR. Nitrogen monoxide (NO) was the first product detected for temperatures higher than 160 °C. The formation of NO is related to the decomposition of residual nitrates belonging to the adsorbent and noble metal precursors that have not been completely decomposed during the calcination step. Then, NH_3 is detected at higher temperatures. The formation of NH_3 by the reduction of residual nitrates requires the noble metal to be in its metallic state, and thus, NH_3 formation can be used as an indirect way to determine the temperature at which ruthenium starts to be reduce. The adsorbent loading influenced the onset of the NH_3 formation and thus the reduction of Ru. NH_3 was detected at 220 °C for the sample containing 5 wt.% of CaO whereas higher temperatures, around 240 °C, were needed for the samples containing 10 and 15 wt.% of CaO. Thus, it can be concluded that the reduction of ruthenium is hindered by the presence of increasing loadings of CaO. This conclusion can be also applied for the samples containing Na_2CO_3 as adsorbent.

Methane formation was also detected during the H_2-TPR. The formation of CH_4 is ascribed to the hydrogenation of the CO_2 adsorbed in the samples, due to the exposure to the environment prior to the experiment. The formation of CH_4 by CO_2 hydrogenation also requires metallic ruthenium. Therefore, the onset temperature for CH_4 detection matches that of NH_3. CH_4 formation was delayed to higher temperatures with increasing the adsorbent loading, which confirms that the reduction of ruthenium is progressively hindered by increasing loadings of adsorbent.

The H_2 consumption detected during the H_2-TPR cannot be only related to the reduction of the noble metal ($Ru_xO_y + yH_2 \rightarrow xRu + yH_2O$). The reduction of residual nitrates ($Ca(NO_3)_2 + 8H_2 \rightarrow 2NH_3 + CaO + 5H_2O$) and the methanation of carbonates ($CaCO_3 + 4H_2 \rightarrow CaO + CH_4 + 2H_2O$) also contribute to the total H_2 consumption. Thus, the overall increase in the H_2 consumption during the H_2-TPR for increasing adsorbent loadings can be related to a higher production of methane due to preadsorbed CO_2 in the samples. Besides, the displacement of the H_2 consumption to higher temperatures is linked to a progressive delay in the temperature at which Ru is reduced.

Taking into account that nitrogen or carbon containing products were not detected during the H_2-TPR for the adsorbent free 4%Ru/Al_2O_3 sample (Figure S3), the H_2 consumption can be exclusively related to the reduction of the noble metal. After integrating and quantifying the hydrogen consumption, the H_2/Ru ratio resulted in 2.0. This result is in agreement with a Ru oxidation state of +4, i.e. RuO_2 ($RuO_2 + 2H_2 \rightarrow Ru + 2H_2O$). The oxidation state of Ru for the samples containing the adsorbent was determined by XPS (Figure S4). For all samples, the XPS spectra were consistent with the presence of Ru^{+4}.

3.4. Temperature programmed surface reaction (TPSR) of pre-adsorbed CO_2 with H_2

Fig. 5 shows the production of CH_4 during temperature programmed surface reaction (TPSR) of pre-adsorbed CO_2 with H_2. These experiments were performed by first reducing the catalyst up to 400 °C with 5%H_2/Ar to clean the catalyst surface and reduce the noble metal to Ru^0. Then, the catalyst was saturated with CO_2 at 50 °C, and finally 5% H_2/Ar gas stream was contacted while increasing the catalyst

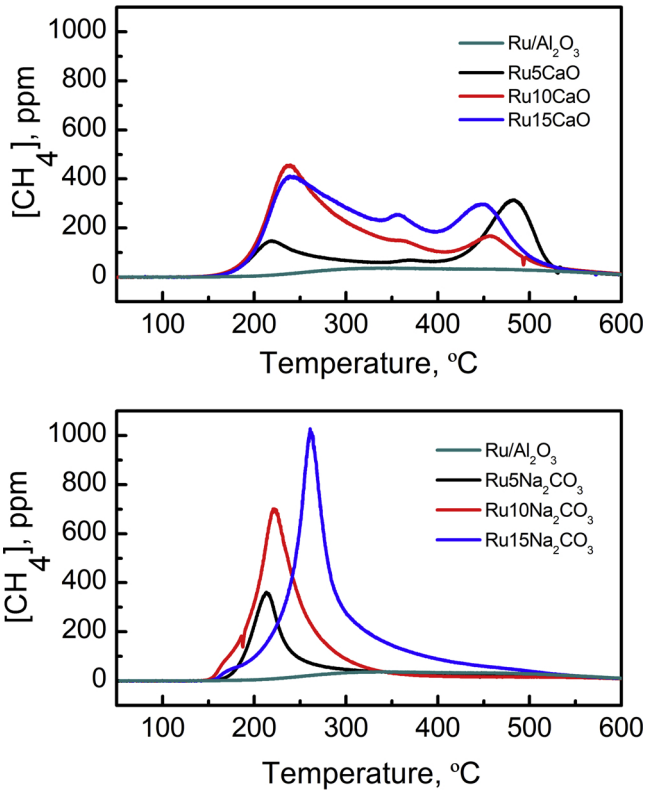

Fig. 5. CH_4 formation during temperature programmed surface reaction with pre-adsorbed CO_2 onto Ru-CaO/Al_2O_3 (a) and Ru-Na_2CO_3/Al_2O_3 (b) samples with different adsorbent contents, i.e. 5, 10 and 15 wt.%. Ru/Al_2O_3 sample is also included as reference.

Table 4
CH_4 formation during TPSR experiments with pre-adsorbed CO_2.

Sample	CH_4, μmol g^{-1}	CH_4/CaO or CH_4/Na_2CO_3
Ru5CaO	396	0.33
Ru10CaO	683	0.32
Ru15CaO	794	0.26
$Ru5Na_2CO_3$	243	0.29
$Ru10Na_2CO_3$	462	0.38
$Ru15Na_2CO_3$	686	0.41
Ru/Al_2O_3	103	–

temperature to 600 °C. In the absence of an adsorbent, i.e. Ru/Al_2O_3 sample, the formation of CH_4 is minor (103 μmol g^{-1}, Table 4), due to the low ability of the sample to pre-adsorb CO_2, as observed in the CO_2-TPD experiment. Table 4 summarizes CH_4 formation during TPSR experiments with all prepared samples.

Catalysts containing CaO as adsorbent presented two different temperature regions for carbonates decomposition and CH_4 production. The low temperature CH_4 production is ascribed to the methanation of the CO_2 adsorbed onto weak basic storage sites, whereas the high temperature production is ascribed to the hydrogenation of the CO_2 adsorbed onto strong basic sites forming very stable carbonates. Note that CH_4 formation is observed even at temperatures as high as 500 °C, which highlights the great stability of the carbonates. Indeed, these results reveal that the complete decomposition of carbonates will not be achieved during the CO_2 adsorption and hydrogenation cycles carried out in section 3.7. CH_4 production clearly increases with the CaO loading, i.e. 396 μmol, 683 μmol and 794 μmol for 5, 10 and 15%, respectively. The adsorbent utilization evaluated as the CH_4/CaO ratio is slightly reduced while increasing the adsorbent loading. The close contact between the storage component and the noble metal has been regarded as a key factor to efficiently decompose and reduce the adsorbed compounds, as observed in the NO_x storage and reduction technology with Pt-BaO/Al_2O_3 catalysts [47,48]. The highest CH_4/CaO ratio (0.33) is observed for the Ru5CaO sample, due to the higher dispersion of Ru (13.1%, Table 2). The close contact between the CaO and Ru promotes the decomposition of carbonates to form gaseous CO_2 that is hydrogenated onto a neighborhood Ru. Decreasing the Ru dispersion results in a progressive reduction of the CH_4/CaO ratio to 0.32 and 0.26 for Ru10CaO and Ru15CaO samples, respectively.

On the other hand, catalysts containing Na_2CO_3 as adsorbent presented a unique temperature region for carbonates decomposition and CH_4 production. Besides, CH_4 formation was detected at temperatures notably lower than CaO containing catalysts, which points out that carbonates formation onto Na_2CO_3 are less stable under a net reducing environment. CH_4 production clearly increases with the Na_2CO_3 loading, i.e. 243 μmol, 462 μmol and 686 μmol for 5, 10 and 15%, respectively. Maximum CH_4/Na_2CO_3 ratio is obtained for the sample with the highest adsorbent loading, i.e. $Ru15Na_2CO_3$, in line with the higher Ru dispersion (19.3%, Table 2).

3.5. CO_2 adsorption and hydrogenation mechanism onto Ru-CaO/Al_2O_3 and Ru-Na_2CO_3/Al_2O_3 catalysts

Fig. 6 shows the concentration profiles of CO_2, H_2O, CH_4 and CO at the reactor outlet for one CO_2 adsorption and hydrogenation cycle, once the steady state was reached. Fig. 6a represents the operation at 370 °C for the Ru10CaO sample, whereas Fig. 6b for the $Ru10Na_2CO_3$ sample. The adsorption and hydrogenation cycle is performed by admitting to the reactor a gas stream composed of 1.4% CO_2/Ar during 1 min. Afterwards, the reactor is purged with Ar for 2 min. Finally, the hydrogenation step is carried out with a gas stream composed of 10%H_2/Ar for 2 min. Fig. 6 also includes the CO_2 concentration profile when the reactor is bypassed.

As can be observed in Fig. 6a, the CO_2 concentration at the reactor outlet remains negligible at the beginning of the storage step. The CO_2 adsorption process onto calcium oxide has been usually described by the following reaction [49,50]:

$$CaO + CO_2 \leftrightarrows CaCO_3 \quad (6)$$

The onset of the CO_2 concentration profile is detected after 25 s, revealing that the adsorption sites became progressively saturated and some CO_2 started to leave the reactor without being stored. Meanwhile H_2O was detected at the reactor outlet. This fact reveals that H_2O is being desorbed from the storage sites while the storage of CO_2 proceeds. The adsorption of CO_2 accompanied by the release of water can be explained by considering the carbonation of hydrated calcium oxide, as follows:

$$Ca(OH)_2 + CO_2 \leftrightarrows CaCO_3 + H_2O \quad (7)$$

Thus, experimental evidences suggest that CaO and $Ca(OH)_2$ coexist in the catalyst surface and both are active sites for the storage of CO_2. Besides, due to the fact that H_2O is not detected at the beginning of the storage period, it can be concluded that the adsorption of CO_2 occurs preferentially onto CaO through Eq. (6) Then, once the CaO sites are occupied, the adsorption can proceed through Eq. (7) by the adsorption of CO_2 onto hydrated $Ca(OH)_2$ and the release of H_2O.

The temporal evolution of reactants and products is qualitatively similar during the CO_2 adsorption and hydrogenation cycles with $Ru10Na_2CO_3$ sample (Fig. 6b). However, the adsorption chemistry is not so well understood for sodium carbonate. As already observed for calcium oxide containing catalysts, at the beginning of the storage period, the concentration of CO_2 is negligible. In this period of time the adsorption of CO_2 is complete and H_2O is not observed in the effluent gas. The following reactions can be used to describe the adsorption of CO_2 without the release of H_2O for sodium containing catalysts:

$$Na_2O + CO_2 \leftrightarrows Na_2CO_3 \quad (8)$$

$$NaOH + CO_2 \leftrightarrows NaHCO_3 \quad (9)$$

Eq. (8) describes the adsorption of CO_2 onto sodium oxide to form sodium carbonate, whereas Eq. (9) yields sodium bicarbonate through carbonation of hydrated sodium oxide. After 30 s of storage time, the adsorption of CO_2 then proceeds with the release of H_2O. The following reaction can be used to describe the adsorption of CO_2 while H_2O is desorbed:

$$2NaOH + CO_2 \leftrightarrows Na_2CO_3 + H_2O \quad (10)$$

As H_2O release is only observed for storage periods longer than 30 s, the extension of Eq. (10) is negligible for shorter storage times. Consequently, as Eq. (9) shares the same reactants than Eq. (10), it can be concluded that the extension of Eq. (9) would be also negligible for short storage periods. Therefore, Eq. (8) results in the unique plausible reaction to describe the CO_2 storage without the release of H_2O during the beginning of the storage step. For longer storage times, once Eq. (10) is running and H_2O and CO_2 are present in the gas stream, the storage of CO_2 could further proceed through the following reaction:

$$Na_2CO_3 + H_2O + CO_2 \leftrightarrows 2NaHCO_3 \quad (11)$$

where the joint adsorption of CO_2 and H_2O onto sodium carbonate yields sodium bicarbonate. The combination of Eqs. (10) and (11) results in Eq. (9), which describes the CO_2 adsorption without the release of H_2O, i.e. H_2O formed through Eq. (10) would be readsorbed to form sodium bicarbonate through Eq. (11). As H_2O formation has been experimentally observed at the reactor outlet, Eq. (11) is discarded to describe the adsorption of CO_2 onto sodium containing catalysts.

To sum up, the storage of CO_2 is carried out over Na_2O and NaOH species. The presence of Na_2O species in alumina supported samples has been already reported by Nguyen et al. [51]. First, more reactive Na_2O species adsorbed CO_2 through Eq. (8) to form Na_2CO_3. Then, when Na_2O species are completely carbonated, the storage of CO_2 can proceed onto NaOH species through Eq. (10), which results in the

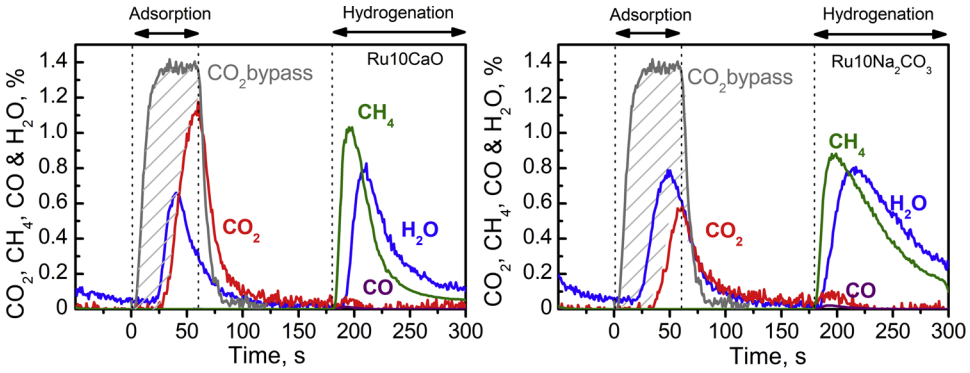

Fig. 6. CO_2, H_2O, CH_4 and CO concentration profiles during one CO_2 adsorption and hydrogenation cycle at 370 °C with Ru10CaO and Ru10Na_2CO_3 samples.

formation of Na_2CO_3 and the release of H_2O. The formation of sodium bicarbonates ($NaHCO_3$) on the catalyst surface through Eqs. (9) and (11) cannot be ruled out, although the extension of those reactions is limited with respect to Eqs. (8) and (10), which are the main reactions to describe the CO_2 adsorption process based on the temporal evolution of reactants and products shown in Fig. 6. In fact, the presence of sodium bicarbonates has only been confirmed by FTIR at room temperature onto samples with low Na_2CO_3 content (< 3 wt.%) [52,53]. It seems that those bicarbonates are easily decomposed to Na_2CO_3 at higher temperatures through the reverse Eq. (11).

The amount of CO_2 adsorbed onto the catalyst is calculated by Eq. (2). During the storage period, 337 and 420 μmol of CO_2 are stored in the Ru10CaO and Ru10Na_2CO_3 catalysts, respectively. After the storage period, the CO_2 is removed from the feed stream and the catalyst is purged with Ar for two minutes, observing that the CO_2 concentration progressively decreases to practically zero. During this period of time, some of the CO_2 physically adsorbed is released. Consequently, the amount of CO_2 adsorbed before the hydrogenation step is slightly reduced to 253 and 391 μmol of CO_2.

Finally, the hydrogenation period begins by feeding a gas stream composed of 10% H_2/Ar with a duration of 2 min. The addition of H_2 in the gas stream reduces the stability of the carbonates and favors their decomposition and subsequent conversion to CH_4 on Ru sites. The formation of CH_4 is immediately detected once H_2 is admitted to the reactor, whereas H_2O formation is delayed around 20 s. The temporal evolution of CH_4 and H_2O can be described by the following reaction scheme:

Step 1: $CaCO_3 \leftrightarrows CaO+CO_2$ (12)

Step 2: $CO_2+4H_2 \leftrightarrows CH_4+2H_2O$ (1)

Step 3: $CaO+H_2O \leftrightarrows Ca(OH)_2$ (13)

Global: $CaCO_3+4H_2 \leftrightarrows Ca(OH)_2+CH_4 + H_2O$ (14)

First, calcium carbonate is decomposed to form gaseous CO_2 (Eq. (12), reverse Eq. (6)). Then, CO_2 reacts with hydrogen to form methane and water Eq. (1). Finally, water is adsorbed on CaO to form $Ca(OH)_2$ Eq. (13). Note that the CO_2 hydrogenation reaction Eq. (1) yields 2 molecules of H_2O per molecule of CH_4. However, comparable amounts of CH_4 and H_2O are experimentally detected at the reactor outlet during the hydrogenation step. This fact, along with the delay in the detection of H_2O with respect to CH_4, strongly suggests that water is being adsorbed in the storage sites Eq. (13) as it is formed through the CO_2 hydrogenation Eq. (1). The hydration of CaO in the presence of water to form $Ca(OH)_2$ has been already described in the literature [54,55].

Thus, the overall hydrogenation process can be described by Eq. (14), involving the reaction of $CaCO_3$ with H_2 to yield hydrated Ca $(OH)_2$, CH_4 and H_2O. This mechanism is consistent with the amount of CO_2 and H_2O detected at the reactor outlet during the hydrogenation step. In fact, 272 μmol of CH_4 and 287 μmol of H_2O are produced for the CaO containing catalyst. The experimental H_2O/CH_4 ratio results in 1.05, very close to that predicted by the stoichiometry of Eq. (14), which validates the proposed reaction to describe the CO_2 decomposition and hydrogenation.

A very small amount of CO (4 μmol) is produced through the RWGS reaction ($CO_2+H_2 \leftrightarrows CO+H_2O$) during the CO_2 hydrogenation step. The amount of CO_2 stored during the adsorption step and the amount of CH_4, H_2O and CO produced during the hydrogenation step are collected in Table 5.

A similar reaction scheme can be deduced for Na_2CO_3 decomposition and hydrogenation as follows, which is also consistent with the experimental data:

Step 1: $Na_2CO_3 \leftrightarrows Na_2O+CO_2$ (15)

Step 2: $CO_2+4H_2 \leftrightarrows CH_4+2H_2O$ (1)

Step 3: $Na_2O+H_2O \leftrightarrows 2NaOH$ (16)

Global: $Na_2CO_3+4H_2 \leftrightarrows 2NaOH+CH_4 + H_2O$ (17)

The CO_2 decomposition and CH_4 formation is slower for Na_2CO_3 containing catalysts. Note that CH_4 formation peaks at lower concentration and widens with respect to CaO containing catalysts. The

Table 5
Stored CO_2 and released H_2O during the adsorption step and CH_4, H_2O and CO production during the hydrogenation step.

Sample	Storage period				*Hydrogenation period*		
	Stored CO_2[a], μmol g^{-1}	Released CO_2[b], μmol g^{-1}	Stored CO_2[c], μmol g^{-1}	ReleasedH_2O[d], μmol g^{-1}	CH_4, μmol g^{-1}	H_2O, μmol g^{-1}	CO, μmol g^{-1}
Ru10CaO	337	84	253	181	272	287	2
Ru10Na_2CO_3	420	29	391	248	398	455	4

[a] Stored CO_2 during the CO_2 adsorption step.
[b] Released CO_2 during the purge step with Ar between storage and hydrogenation periods.
[c] Stored CO_2 before the hydrogenation step.
[d] Released H_2O during the CO_2 adsorption step and the purging step.

slower CH_4 formation kinetics would have practical implications for the industrial application and would imply the adjustment of the hydrogenation period time for an efficient use of the reductant.

In this case, 398 μmol of CH_4 and 454 μmol of H_2O are produced during the hydrogenation step and the H_2O/CH_4 ratio results in 1.14, which is also close to the stoichiometry of Eq. (17), and again validates the proposed mechanism to describe the CO_2 adsorption and hydrogenation with Na_2CO_3 containing catalyst. Preliminary experiments by FTIR further corroborate the proposed mechanism for the CO_2 storage and hydrogenation (Figure S5).

Finally, if the CO_2 adsorption and hydrogenation periods are jointly considered, the combination of Eqs. (7) and (14) for CaO containing catalysts and the combination of Eqs. (10) and (17) results in the CO_2 hydrogenation reaction, i.e. Eq. (1). Integrating the H_2O formation in both periods the result obtained is 468 and 703 μmol of H_2O for CaO and Na_2CO_3 containing catalysts, respectively. Thus, the H_2O/CH_4 ratio results in 1.72 and 1.76, close to the value of 2 predicted by the stoichiometry of the CO_2 hydrogenation reaction (Eq. 1). The carbon balance was also adequately closed. The amount of CO_2 stored during the adsorption period is 391 μmol, while 398 μmol of CH_4 and 4 μmol of CO are produced during the CO_2 hydrogenation for CaO containing catalyst, which closes the carbon balance in 103%. The formation of other carbon-based products than CH_4 or CO, such as C_2H_6, C_2H_4, C_2H_2 or CH_2O was experimentally discarded by FTIR. In the same line, 253 μmol of CO_2 are stored and 272 μmol of CH_4 and 2 μmol of CO produced for Na_2CO_3 containing catalyst, which closes the carbon balance in 108%.

3.6. Adsorbent loading and temperature effects on CO_2 adsorption and hydrogenation cycles

Similar CO_2 adsorption and hydrogenation cycles have been performed with all the prepared samples in the temperature range of 280–400 °C. For these experiments, the CO_2 concentration at the reactor inlet during the storage step has been set at 11% in order to mimic an effluent gas from a combustion process. The CO_2 adsorption and hydrogenation cycles can be observed in Figure S6. The amount of CO_2 stored and the amount of CH_4 and CO produced have been calculated through Eqs. (2)–(3), respectively, and results are collected in Fig. 7.

As a general trend, the amount of CH_4 produced during the hydrogenation step (Fig. 7b) is very close to the amount of CO_2 stored during the adsorption step (Fig. 7a), and the amount of CO produced is minor. The carbon balance for all the experiments closes within ± 5%.

The highest CH_4 production for a low adsorbent loading, either 5%CaO or 5%Na_2CO_3, is observed at low temperature, i.e. 280 °C. Then, a decreasing tendency is observed while the reaction temperature is increased. The same trend is observed for the storage of CO_2. These results can be linked with the basicity of the samples. Indeed, the CO_2-TPD experiments revealed that the weak basicity was the main contribution to the total basicity and that strong basicity was almost negligible in the case of samples with a low adsorbent loading. Thus, the CO_2 adsorption capacity is higher at low temperature because the weak basicity participates in the storage of CO_2. On the contrary, the CO_2 adsorption capacity is lower at higher temperature because the weak storage sites do not have enough strength to capture CO_2 and strong storage sites are absent in the samples. The maximum CO_2 storage and CH_4 production is slightly higher for Na_2CO_3 containing catalysts due to the higher amount of weak basicity with respect to CaO containing catalysts (Table 3), which promotes the CO_2 adsorption.

Increasing the adsorbent loading to 10% and 15% results in a clear promotion of the CO_2 storage and CH_4 production. However, some differences are observed among the different adsorbent types. In the case of CaO, the CO_2 storage and CH_4 production clearly increases with temperature, as opposite to that observed for the sample with a low adsorbent content. Minimum CH_4 production and CO_2 storage is observed at low temperature (280 °C). Note that increasing the adsorbent loading to 10 or 15% progressively promotes the formation of strong basic sites, as observed in the CO_2-TPD. Thus, the adsorption of CO_2 onto strong basic sites results in the formation of very stable carbonates that do not decompose even in the presence of a reducing environment (10%H_2/Ar). In fact, TPSR experiments revealed that CH_4 formation was observable up to 500 °C, i.e. high temperature was needed to completely decompose the carbonates. Thus, increasing the reaction temperature progressively facilitates a deeper regeneration of the catalyst and consequently higher amount of storage sites are available to capture CO_2 in the subsequent storage period. In line with the previous explanation, maximum CH_4 production of 259 μmol and 414 μmol is observed at the highest temperature (400 °C) for adsorbent loadings of 10 and 15%, respectively. In summary, CH_4 production is favored for high adsorbent loadings and elevated temperatures in the case of CaO.

Temperature effect is not so noteworthy in the production of CH_4 for catalysts containing 10% and 15% Na_2CO_3. It has been observed by CO_2-TPD experiments that strong basic sites are not so abundant and the strength of those sites is smaller in the case of Na_2CO_3 with respect to CaO. Furthermore, TPSR experiments revealed that the regeneration of the storage sites could be obtained at much lower temperature, with CH_4 production peak situated around 300 °C. Thus, the decomposition of carbonates is not a limiting factor and high CO_2 adsorption and methanation capacity is observed even at low temperature, as opposite to catalysts containing CaO as adsorbent. Maximum CH_4 production is observed at intermediate temperature (340 °C), which could be attributed to a slightly deeper regeneration of the storage sites. Then, a further temperature increase penalizes CH_4 production because the number of basic storage sites with enough strength to participate in the CO_2 adsorption is reduced. The higher dispersion of the Ru for Na_2CO_3 containing samples also has a positive effect in CH_4 production, especially at low temperatures, with respect to CaO containing catalysts.

CO formation is always minor with respect to CH_4 irrespective the reaction temperature and the adsorbent nature and loading. CO formation tends to increase with the reaction temperature due to the promotion of the RWGS ($CO_2 + H_2 \leftrightarrows CO + H_2O$) during the CO_2 hydrogenation step.

Finally, the stability of Ru10Na_2CO_3 sample was studied performing 15 consecutive adsorption and hydrogenation cycles at 400 °C (Figure S7). The evolution of CO_2, CH_4 and H_2O was repetitive during the 15 consecutive cycles. CH_4 yield per cycle remained constant, highlighting the stability of the catalyst towards the CO_2 adsorption and methanation reaction.

4. Conclusions

Ru-CaO/Al_2O_3 and Ru-Na_2CO_3/Al_2O_3 catalysts with different adsorbent loadings, i.e. 5, 10 and 15%, have been synthesized for the CO_2 storage and in situ hydrogenation to CH_4. As the adsorbent content increases, the specific surface area of the catalyst decreases. Besides, in the case of CaO, it hinders the correct dispersion of the noble metal, and therefore, lower Ru dispersion is obtained for high adsorbent contents, proven by H_2 chemisorption and TEM microscopy. This tendency is opposite to that observed for catalysts containing Na_2CO_3, since higher contents have a promoter effect and facilitate the dispersion of Ru.

The total basicity of the samples is promoted with increasing the adsorbent loading. Weak basicity is predominant for low adsorbent loadings, whereas strong basicity becomes principal for higher contents. Furthermore, the strength of the strong basicity is enhanced with the adsorbent loading due to the formation of highly stable carbonates. Specifically, the strength of the strong basicity is higher for CaO with respect to Na_2CO_3. Consequently, higher reduction temperatures are required during TPSR experiments to promote the decomposition and hydrogenation of the CO_2 adsorbed onto CaO. In fact, CH_4 formation was observable up to 500 °C. On the other hand, 300 °C was enough to promote the decomposition of carbonates and CH_4 formation in the case of Na_2CO_3 containing catalysts. Besides, Ru dispersion also

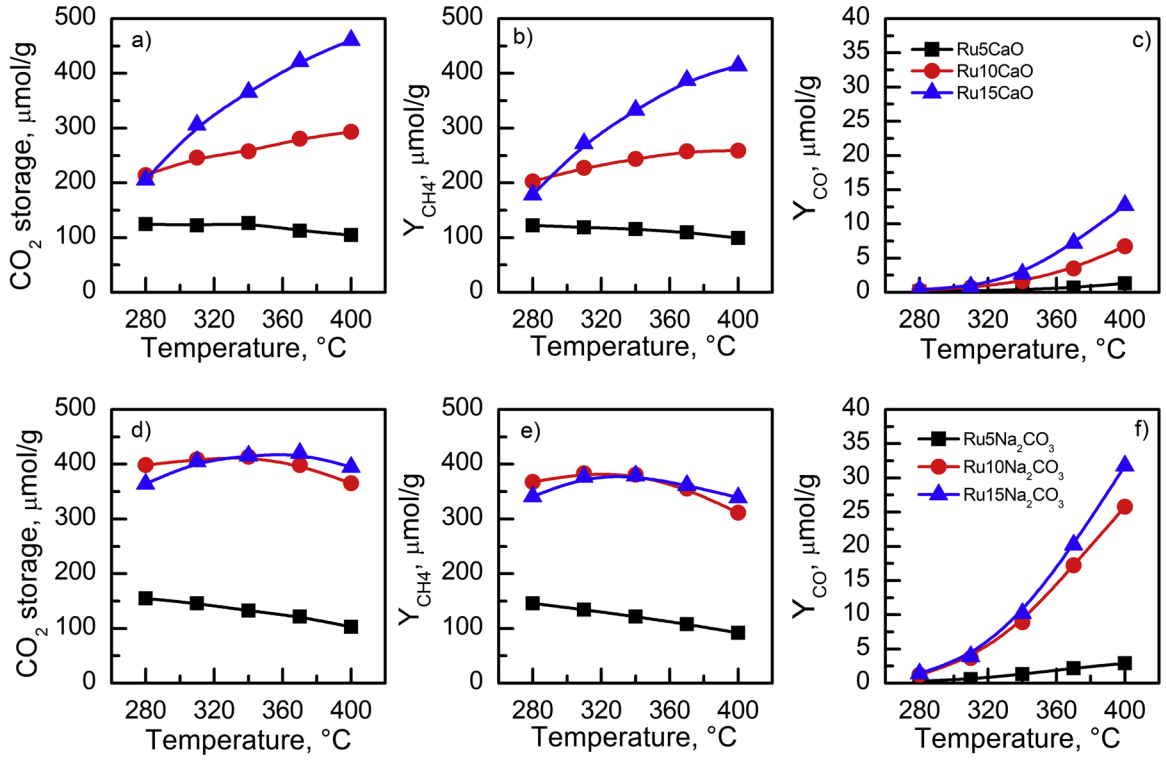

Fig. 7. Evolution of CO_2 storage and CH_4 and CO productions with temperature for Ru-CaO/Al_2O_3 (a, b, c, respectively) and Ru-Na_2CO_3/Al_2O_3 (d, e, f, respectively) samples with different adsorbent contents, i.e. 5, 10 and 15 wt.%.

facilitates the decomposition of carbonates and the formation of CH_4.

A complete reaction scheme describing the CO_2 adsorption and hydrogenation process has been proposed. Total CO_2 adsorption has been observed in the beginning of the storage period. Afterwards, the CO_2 adsorption proceeds with the release of H_2O; CaO and $Ca(OH)_2$ species have been identified as CO_2 storage sites. The adsorption occurs preferentially onto CaO and once those sites are occupied, the adsorption can proceed onto $Ca(OH)_2$ by the release of H_2O. The same is applied for Na_2CO_3 containing catalysts. The CO_2 is preferentially adsorbed onto Na_2O species and then onto NaOH with the release of H_2O. During the hydrogenation step, CH_4, H_2O and CO are detected. The detection of H_2O is delayed with respect to the beginning of the hydrogenation period, suggesting that H_2O formed through the CO_2 hydrogenation is adsorbed onto the storage sites. CO formation is minor irrespective of the nature of the adsorbent, which highlights the high selectivity of the prepared catalysts towards CH_4 formation.

The CO_2 storage capacity and CH_4 production is penalized with increasing the reaction temperature for low adsorbent loading samples, either CaO or Na_2CO_3. As those samples only presented weak basicity, the ability to store CO_2 decreased with increasing temperature. Higher adsorbent loadings promote the CO_2 storage and methanation. Some differences were observed between the CO_2 adsorption and hydrogenation performance for CaO and Na_2CO_3. In the case of CaO, the formation of stable carbonates requires higher temperatures to adequately regenerate the catalyst during the hydrogenation step. Consequently, CH_4 formation is promoted with temperature. On the other hand, the stability of carbonates is lower for Na_2CO_3, promoting CH_4 formation at intermediate temperatures.

Acknowledgements

The financial support from the Economy and Competitiveness Spanish Ministry (CTQ2015-67597-C2-1-R) and the Basque Government (IT657-13 and IT1297-19) is acknowledged. The authors thank for technical and human support provided by SGIker (UPV/EHU Advanced Research Facilities/ ERDF, EU). One of the authors (ABL) also acknowledges the Economy and Competitiveness Spanish Ministry for his PhD grant (BES-2016-077855).

Appendix A. Supplementary data

Supplementary material related to this article can be found, in the online version, at doi:https://doi.org/10.1016/j.apcatb.2019.117845.

References

[1] M.D. Aminu, S.A. Nabavi, C.A. Rochelle, V. Manovic, A review of developments in carbon dioxide storage, Appl. Energy 208 (2017) 1389–1419.
[2] M.D. Porosoff, B. Yan, J.G. Chen, Catalytic reduction of CO_2 by H_2 for synthesis of CO, methanol and hydrocarbons: challenges and opportunities, Energy Environ. Sci. 9 (2016) 62–73.
[3] C. Janke, M.S. Duyar, M. Hoskins, R. Farrauto, Catalytic and adsorption studies for the hydrogenation of CO_2 to methane, Appl. Catal. B: Environ. 152-153 (2014) 184–191.
[4] S. Saeidi, N.A.S. Amin, M.R. Rahimpour, Hydrogenation of $CO_2$to value-added products - a review and potential future developments, J. CO_2 Util. 5 (2014) 66–81.
[5] W. Wang, S. Wang, X. Ma, J. Gong, Recent advances in catalytic hydrogenation of carbon dioxide, Chem. Soc. Rev. 40 (2011) 3703–3727.
[6] N.A. Rashidi, S. Yusup, An overview of activated carbons utilization for the post-combustion carbon dioxide capture, J. CO_2 Util. 13 (2016) 1–16.
[7] S. Selosse, O. Ricci, Carbon capture and storage: lessons from a storage potential and localization analysis, Appl. Energy 188 (2017) 32–44.
[8] A. Evans, V. Strezov, T.J. Evans, Assessment of utility energy storage options for increased renewable energy penetration, Renew. Sustain. Energy Rev. 16 (2012) 4141–4147.
[9] F. Ocampo, B. Louis, L. Kiwi-Minsker, A. Roger, Effect of Ce/Zr composition and noble metal promotion on nickel based $Ce_xZr1_{-x}O_2$ catalysts for carbon dioxide methanation, Appl. Catal. A Gen. 392 (2011) 36–44.
[10] J.C. Matsubu, V.N. Yang, P. Christopher, Isolated metal active site concentration and stability control catalytic CO_2 reduction selectivity, J. Am. Chem. Soc. 137 (2015) 3076–3084.
[11] J. Graciani, K. Mudiyanselage, F. Xu, A.E. Baber, J. Evans, S.D. Senanayake, D.J. Stacchiola, P. Liu, J. Hrbek, J. Fernández Sanz, J.A. Rodriguez, Highly active copper-ceria and copper-ceria-titania catalysts for methanol synthesis from CO_2, Science. 345 (2014) 546–550.
[12] G. Laurenczy, Hydrogen storage and delivery: the carbon dioxide - Formic acid couple, Chimia 65 (2011) 663–666.

[13] M.- Fan, A.Z. Abdullah, S. Bhatia, Catalytic technology for carbon dioxide reforming of methane to synthesis gas, ChemCatChem. 1 (2009) 192–208.
[14] M. Aresta, A. Dibenedetto, Utilisation of CO_2 as a chemical feedstock: opportunities and challenges, Dalton Trans. (2007) 2975–2992.
[15] C. Song, Global challenges and strategies for control, conversion and utilization of CO_2 for sustainable development involving energy, catalysis, adsorption and chemical processing, Catal. Today 115 (2006) 2–32.
[16] P. Sabatier, J.B. Senderens, New synthesis of methane, J. Chem. Soc., Faraday Trans. 82 (1902) 333–337.
[17] Audi unveils h-tron quattro concept car at Detroit auto show, Fuel Cells Bull. 2016 (2016) 2.
[18] K.P. Brooks, J. Hu, H. Zhu, R.J. Kee, Methanation of carbon dioxide by hydrogen reduction using the Sabatier process in microchannel reactors, Chem. Eng. Sci. 62 (2007) 1161–1170.
[19] D.C.D. Da Silva, S. Letichevsky, L.E.P. Borges, L.G. Appel, The Ni/ZrO_2 catalyst and the methanation of CO and CO_2, Int. J. Hydrogen Energ. 37 (2012) 8923–8928.
[20] F. Mohseni, M. Magnusson, M. Görling, P. Alvfors, Biogas from renewable electricity Increasing a climate neutral fuel supply, Appl. Energy 90 (2012) 11–16.
[21] S. Takenaka, T. Shimizu, K. Otsuka, Complete removal of carbon monoxide in hydrogen-rich gas stream through methanation over supported metal catalysts, Int. J. Hydrogen Energy 29 (2004) 1065–1073.
[22] Y. Zhou, Y. Jiang, Z. Qin, Q. Xie, H. Ji, Influence of Zr, Ce, and La on Co_3O_4 catalyst for CO_2 methanation at low temperature, Chin. J. Chem. Eng. 26 (2018) 768–774.
[23] A.H. Zamani, R. Ali, W.A.W.A. Bakar, The investigation of $Ru/Mn/Cu–Al_2O_3$ oxide catalysts for CO_2/H_2 methanation in natural gas, J. Taiwan Inst. Chem. Eng. 45 (2014) 143–152.
[24] A. Lazdans, E. Dace, J. Gusca, Development of the experimental scheme for methanation process, Energy Proced. 95 (2016) 540–545.
[25] C. Song, W. Pan, Tri-reforming of methane: a novel concept for catalytic production of industrially useful synthesis gas with desired H_2/CO ratios, Catal. Today 98 (2004) 463–484.
[26] M. Minutillo, A. Perna, A novel approach for treatment of CO_2 from fossil fired power plants, Part A: the integrated systems ITRPP, Int. J. Hydrogen Energy 34 (2009) 4014–4020.
[27] M.S. Duyar, M.A.A. Treviño, R.J. Farrauto, Dual function materials for CO_2 capture and conversion using renewable H_2, Appl. Catal. B: Environ. 168-169 (2015) 370–376.
[28] J.V. Veselovskaya, P.D. Parunin, A.G. Okunev, Catalytic process for methane production from atmospheric carbon dioxide utilizing renewable energy, Catal. Today 298 (2017) 117–123.
[29] J.V. Veselovskaya, P.D. Parunin, O.V. Netskina, L.S. Kibis, A.I. Lysikov, A.G. Okunev, Catalytic methanation of carbon dioxide captured from ambient air, Energy 159 (2018) 766–773.
[30] P. Melo Bravo, D.P. Debecker, Combining CO_2 capture and catalytic conversion to methane, Waste Disposal Sustain. Energy 1 (2019) 53–65.
[31] C.V. Miguel, M.A. Soria, A. Mendes, L.M. Madeira, A sorptive reactor for CO_2 capture and conversion to renewable methane, J. Chem. Eng. 322 (2017) 590–602.
[32] J.V. Veselovskaya, P.D. Parunin, O.V. Netskina, A.G. Okunev, A novel process for renewable methane production: combining direct air capture by K_2CO_3/alumina sorbent with CO_2 methanation over Ru/alumina catalyst, Top. Catal. 61 (2018) 1528–1536.
[33] Q. Zheng, R. Farrauto, A. Chau Nguyen, Adsorption and Methanation of Flue Gas CO_2 with Dual Functional Catalytic Materials: A Parametric Study, Ind. Eng. Chem. Res. 55 (2016) 6768–6776.
[34] M.S. Duyar, S. Wang, M.A. Arellano-Treviño, R.J. Farrauto, CO_2utilization with a novel dual function material (DFM) for capture and catalytic conversion to synthetic natural gas: an update, J. CO_2 Util. 15 (2016) 65–71.
[35] L.F. Bobadilla, J.M. Riesco-García, G. Penelás-Pérez, A. Urakawa, Enabling continuous capture and catalytic conversion of flue gas $CO_2$to syngas in one process, J. CO_2 Util. 14 (2016) 106–111.
[36] S. Wang, R.J. Farrauto, S. Karp, J.H. Jeon, E.T. Schrunk, Parametric, cyclic aging and characterization studies for CO_2 capture from flue gas and catalytic conversion to synthetic natural gas using a dual functional material (DFM), J. CO_2 Util. 27 (2018) 390–397.
[37] P. Gruene, A.G. Belova, T.M. Yegulalp, R.J. Farrauto, M.J. Castaldi, Dispersed calcium oxide as a reversible and efficient CO2 − sorbent at intermediate temperatures, Ind. Eng. Chem. Res. 50 (2011) 4042–4049.
[38] B. Zhao, D. Jiang, Y. Xie, Dispersion of Na_2CO_3 on γ-Al_2O_3 and the threshold effect in flue-gas desulfurization, Fuel 81 (2002) 1565–1568.
[39] N. Pasupulety, K. Gunda, Y. Liu, G.L. Rempel, F.T.T. Ng, Production of biodiesel from soybean oil on CaO/Al_2O_3 solid base catalysts, Appl. Catal. A Gen. 452 (2013) 189–202.
[40] S. Tada, O.J. Ochieng, R. Kikuchi, T. Haneda, H. Kameyama, Promotion of CO_2 methanation activity and CH_4 selectivity at low temperatures over $Ru/CeO_2/Al2O_3$ catalysts, Int. J. Hydrogen Energy 39 (2014) 10090–10100.
[41] J.M. Gatica, R.T. Baker, P. Fornasiero, S. Bernal, J. Kašpar, Characterization of the metal phase in $NM/Ce_{0.68}Zr_{0.32}O_2$(NM: Pt and Pd) catalysts by hydrogen chemisorption and HRTEM microscopy: a comparative study, J. Phys. Chem. B 105 (2001) 1191–1199.
[42] B. Pereda-Ayo, U. De La Torre, M.P. González-Marcos, J.R. González-Velasco, Influence of ceria loading on the NO_x storage and reduction performance of model $Pt–Ba/Al_2O_3$ NSR catalyst, Catal. Today 241 (2015) 133–142.
[43] A. Miyazaki, I. Balint, K.- Aika, Y. Nakano, Preparation of Ru nanoparticles supported on γ-Al_2O_3 and its novel catalytic activity for ammonia synthesis, J. Catal. 204 (2001) 364–371.
[44] X. Shen, L. Garces, Y. Ding, K. Laubernds, R.P. Zerger, M. Aindow, E.J. Neth, S.L. Suib, Behavior of H_2 chemisorption on Ru/TiO_2 surface and its application in evaluation of Ru particle sizes compared with TEM and XRD analyses, Appl. Catal. A Gen. 335 (2008) 187–195.
[45] W. Yang, Y. Feng, W. Chu, Promotion effect of CaO modification on mesoporous Al_2O_3-supported Ni catalysts for CO_2 methanation, Int. J. Chem. Eng. 2016 (2016).
[46] M.S. Duyar, A. Ramachandran, C. Wang, R.J. Farrauto, Kinetics of CO_2 methanation over Ru/γ-$Al_2O_3$and implications for renewable energy storage applications, J. CO_2 Util. 12 (2015) 27–33.
[47] N.W. Cant, I.O.Y. Liu, M.J. Patterson, The effect of proximity between Pt and BaO on uptake, release, and reduction of NO_x on storage catalysts, J. Catal. 243 (2006) 309–317.
[48] B. Pereda-Ayo, R. López-Fonseca, J.R. González-Velasco, Influence of the preparation procedure of NSR monolithic catalysts on the Pt-Ba dispersion and distribution, Appl. Catal. A Gen. 363 (2009) 73–80.
[49] J. Phromprasit, J. Powell, S. Assabumrungrat, Metals (Mg, Sr and Al) modified CaO based sorbent for CO2 sorption/desorption stability in fixed bed reactor for high temperature application, Chem. Eng. J. 284 (2016) 1212–1223.
[50] M. Shokrollahi Yancheshmeh, H.R. Radfarnia, M.C. Iliuta, High temperature CO_2 sorbents and their application for hydrogen production by sorption enhanced steam reforming process, Chem. Eng. J. 283 (2016) 420–444.
[51] T.S. Nguyen, L. Lefferts, K.B. Saisankargupta, K. Seshan, Catalytic conversion of biomass pyrolysis vapours over sodium-based catalyst: A study on the state of sodium on the catalyst, ChemCatChem. 7 (2015) 1833–1840.
[52] C.J. Keturakis, F. Ni, M. Spicer, M.G. Beaver, H.S. Caram, I.E. Wachs, Monitoring solid oxide CO_2 capture sorbents in action, ChemSusChem. 7 (2014) 3459–3466.
[53] M. Hartman, K. Svoboda, M. Pohorelý, M. Šyc, Thermal decomposition of sodium hydrogen carbonate and textural features of its calcines, Ind. Eng. Chem. Res. 52 (2013) 10619–10626.
[54] J. Blamey, V. Manovic, E.J. Anthony, D.R. Dugwell, P.S. Fennell, On steam hydration of CaO-based sorbent cycled for CO_2 capture, Fuel 150 (2015) 269–277.
[55] Z. Li, Y. Wang, K. Xu, J. Yang, S. Niu, H. Yao, Effect of steam on CaO regeneration, carbonation and hydration reactions for CO_2 capture, Fuel Process. Technol. 151 (2016) 101–106.